MITSUBISHI HEAVY INDUSTRIES, LTD.
16-5, KONAN 2-CHOME, MINATO-KU
TOKYO, JAPAN

February 9, 2011

Document Control Desk
U.S. Nuclear Regulatory Commission
Washington, DC 20555-0001

Attention: Mr. Jeffery A. Ciocco

Docket No. 52-021
MHI Ref: UAP-HF-11028

Subject: MHI's Outputs related to US-APWR DCD RAI No. 636-4732

Reference: 1) "Request for Additional Information No. 636-4732 Revision 0, SRP Section: 03.06.02 – Determination of Rupture Locations and Dynamic Effects Associated with the Postulated Rupture of Piping, Application Section: 3.6.2," dated 9/23/2010.
2) "MHI's Responses to US-APWR DCD RAI No. 636-4732," UAP-HF-10335, dated 12/15/2010.

With this letter, Mitsubishi Heavy Industries, Ltd. ("MHI") transmits to the U.S. Nuclear Regulatory Commission ("NRC") Outputs related to US-APWR DCD RAI No. 636-4732.

Enclosed are 6 references cited in Reference 2, technical report, MUAP-10022-P Revision 0, entitled "Evaluation on Jet Impingement Issues Associated with Postulated Pipe Rupture (Proprietary)", and MUAP-10022-NP Revision 0, entitled "Evaluation on Jet Impingement Issues Associated with Postulated Pipe Rupture (Non-Proprietary)". The Technical Reports is being submitted electronically in compact discs (CDs). These materials were prepared to reflect the discussion results at the conference call with NRC held on December 1. Additionally, remained 10 references were already submitted to NRC with MHI letter (UAP-HF-10356).

The enclosed presentation material and technical report contains information that MHI considers proprietary, and therefore the material and report should be withheld from disclosure pursuant to 10 C.F.R. § 2.390 (a)(4) as trade secrets and commercial or financial information which is privileged or confidential. Accordingly, the Report is being submitted in two versions, in separate compact discs. One version (in CD 1) contains the complete proprietary version of the Report. The non-proprietary version of the Report is enclosed in CD 2. In the non-proprietary version, the proprietary information, bracketed in the proprietary version, is replaced by the designation "[ ]". In accordance with the NRC submittal procedures, this letter includes an Affidavit that identifies the reasons why the proprietary version of the Report should be withheld from disclosure pursuant to 10 C.F.R. § 2.390 (a)(4).

Please contact Dr. C. Keith Paulson, Senior Technical Manager, Mitsubishi Nuclear Energy Systems, Inc. if the NRC has questions concerning any aspect of this submittal. His contact information is provided below.

D081
NRO

Sincerely,

Atsushi Kumaki for

Yoshiki Ogata,
General Manager- APWR Promoting Department
Mitsubishi Heavy Industries, LTD.

Enclosures:

1. Affidavit of Atsushi Kumaki

2. References cited in Response to RAI 636-4732 for Pipe Break Hazard Analysis Revision 1

3. CD 1: Technical Report, MUAP-10022-P Revision 1, "Evaluation on Jet Impingement Issues Associated with Postulated Pipe Rupture (Proprietary)"

4. CD 2: Technical Report, MUAP-10022-NP Revision 1, "Evaluation on Jet Impingement Issues Associated with Postulated Pipe Rupture (Non-Proprietary)"

The file contained in each CD is listed in Attachments 1 hereto.

CC: J. A. Ciocco
C. K. Paulson

Contact Information

C. Keith Paulson, Senior Technical Manager
Mitsubishi Nuclear Energy Systems, Inc.
300 Oxford Drive, Suite 301
Monroeville, PA 15146
E-mail: ck_paulson@mnes-us.com
Telephone: (412) 373-6466

Enclosure 1

Docket No. 52-021
MHI Ref: UAP-HF-11028

MITSUBISHI HEAVY INDUSTRIES, LTD.

AFFIDAVIT

I, Atsushi Kumaki, state as follows:

1. I am Group Manager, Licensing Promoting Group in APWR Promoting Department, of Mitsubishi Heavy Industries, LTD ("MHI"), and have been delegated the function of reviewing MHI's US-APWR documentation to determine whether it contains information that should be withheld from public disclosure pursuant to 10 C.F.R. § 2.390 (a)(4) as trade secrets and commercial or financial information which is privileged or confidential.

2. In accordance with my responsibilities, I have reviewed the enclosed documents, MUAP-10022 Revision 0 and have determined that portions of the document contain proprietary information that should be withheld from public disclosure. All pages contain proprietary information as identified with the label "Proprietary" on the top of the page, and the proprietary information has been bracketed with an open and closed bracket as shown here "[ ]". The first page of the document indicates that all information identified as "Proprietary" should be withheld from public disclosure pursuant to 10 C.F.R. § 2.390 (a)(4).

3. The information identified as proprietary in the enclosed documents has in the past been, and will continue to be, held in confidence by MHI and its disclosure outside the company is limited to regulatory bodies, customers and potential customers, and their agents, suppliers, and licensees, and others with a legitimate need for the information, and is always subject to suitable measures to protect it from unauthorized use or disclosure.

4. The basis for holding the referenced information confidential is that it describes the unique design and methodology developed by MHI for performing the plant design of protection against postulated piping failures.

5. The referenced information is being furnished to the Nuclear Regulatory Commission ("NRC") in confidence and solely for the purpose of information to the NRC staff.

6. The referenced information is not available in public sources and could not be gathered readily from other publicly available information. Other than through the provisions in paragraph 3 above, MHI knows of no way the information could be lawfully acquired by organizations or individuals outside of MHI.

7. Public disclosure of the referenced information would assist competitors of MHI in their design of new nuclear power plants without incurring the costs or risks associated with the design of the subject systems. Therefore, disclosure of the information contained in the referenced document would have the following negative impacts on the competitive position of MHI in the U.S. nuclear plant market:

A. Loss of competitive advantage due to the costs associated with the development of the methodology related to the analysis.

B. Loss of competitive advantage of the US-APWR created by the benefits of the approach to jet expansion modeling that maintains the desired level of conservatism.

I declare under penalty of perjury that the foregoing affidavit and the matters stated therein are true and correct to the best of my knowledge, information and belief.

Executed on this 9th day of February, 2011.

Atsushi Kumaki

Atsushi Kumaki,
Group Manager- Licensing Promoting Group in APWR Promoting Department
Mitsubishi Heavy Industries, LTD.

Enclosure 2

UAP-HF-11028
Docket No. 52-021

References cited in Response to RAI 636-4732 for Pipe Break Hazard Analysis Revision 1

February, 2011
(Non-proprietary)

4.1.2 Perfect reflection of symmetric spherical waves: the principle of reflection

It is generally known[1] that reflection at the air–water interface is nearly perfect. As an example of such a case, let us assume a rigid wall surface and calculate a sound field where there is a pulsating sphere at a distance of h. As shown in Fig. 4.2, A is the location of the sound source, and P is a point in space. If there is no interface, the velocity potential at P of the sound wave emitted from A can be calculated, if the distance between A and P is represented by r_1, as

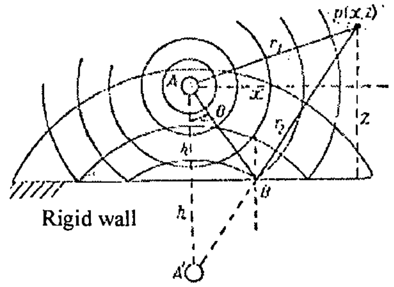

Fig. 4.2

(19) $$\phi_1 = \frac{A}{4\pi r_1} e^{ikr_1}$$

where $A = A_0 e^{-i\omega t}$ is the intensity of the sound source.

If an interface exists, part of the wave front reflected by the interface passes through P. Because the angle of reflection is equal to the angle of incidence, the wave front passes through P as if it was emitted from A', which is an image of the sound source A. What the term "an **image of** A"[2] here means is as follows. Let O' be the foot of the perpendicular drawn from A to the interface, and let A' be a point on the extension of AO so that $OA' = OA$. Then, assume that there is a point sound source $A_0 e^{-i\omega t}$ whose intensity is equal to that of the sound source at A. This is as if an image was produced at A' if the interface was a mirror and A was a light source. In the case of reflection by a rigid wall, it is generally known that the energy of the reflected wave is equal to the energy of the incident wave, and the sign of the velocity potential of the reflected wave does not change. If $A'P$ is represented by r_2, the wave front of the reflected wave passing through P can be expressed as

(20) $$\phi_2 = \frac{A}{4\pi r_2} e^{ikr_2}$$

In the above equation, r_2 is equal to the distance the wave front emitted from A in the direction of θ reflected at B and travels until arriving at P. This result is practically identical to a sound field where the interface has disappeared and there is a sound source at A' in the space filled with a uniform medium.

---

[1] See 3.2.4

[2] image

A sound source at P when there is a wall may be regarded as a synthetic sound field created by the point sound source $A_0e^{-i\omega t}$ at A and the point sound source $A_0e^{-i\omega t}$ at A' when it is assumed that the wall has been removed, and can be expressed as

(21) $$\phi = \frac{Ae^{+ikr_1}}{4\pi r_1} + \frac{Ae^{+ikr_2}}{4\pi r_2}$$

To further simplify Eq. (21), let us assume

(22) $$r_1 + r_2 = 2r,$$

(23) $$r_2 - r_1 = 2s$$

Then, we have

(24) $$4\pi\phi = Ae^{+ikr}\left[\left(\frac{1}{r_2} + \frac{1}{r_1}\right)\cos ks - i\left(\frac{1}{r_1} - \frac{1}{r_2}\right)\sin ks\right]$$

Because $r_1 \approx r_2$ at a point distant from the sound source, the second term is negligibly small compared with the first term. Furthermore, because $\kappa s \ll 1$ holds true if the sound source height h is small relative to the wavelength, the first term can rewritten as

(25) $$4\pi\phi \doteqdot 2A\frac{e^{+ikr}}{r}$$

This indicates that a sound field far from a sound source near a rigid wall is twice as intense as a sound field in the no-wall case. Since, however, actual sound waves are generated only on one side of the wall, the amount of energy required to sustain the vibration of the sound source is twice as large as the amount of energy needed in the no-wall case.

Because the intensity of sound is given in terms of energy flux density, it is proportional to the <u>square of the real number</u> part of the right-hand side of Eq. (24) and can be calculated as

(26) $$A_0^2\left\{\frac{1}{r_1^2} + \frac{1}{r_2^2} + \frac{2}{r_1 r_2}\cos k(r_2 - r_1)\right\}$$

and its magnitude is between

$$A_0^2\left(\frac{1}{r_1} + \frac{1}{r_2}\right)^2 \quad \text{and} \quad A_0^2\left(\frac{1}{r_1} - \frac{1}{r_2}\right)^2$$

<u>If the sound source height h is not small compared with the wavelength</u> λ, $k(r_2 - r_1)$ is large and cannot be ignored. The intensity of sound, therefore, changes according to $(r_2 - r_1)$ and is maximized at

(27) $$\cos k(r_2 - r_1) = +1, \qquad \text{that is} \qquad r_2 - r_1 = \frac{2n\pi}{k} = n\lambda, \qquad n = 0, 1, 2, \cdots$$

and minimized at

(28) $\cos k(r_2 - r_1) = -1,$ that is $r_2 - r_1 = \frac{\left(n+\frac{1}{2}\right)2\pi}{k} = \left(n+\frac{1}{2}\right)\lambda, \quad n=0,1,2,\cdots$

This is the same phenomenon as **Fresnel's interference** mechanism of light.

The same can be said when considering reflection by a water surface in the case where there is an underwater sound source. In that case, however, the phase of the reflected wave is reversed because the reflecting surface is not a rigid wall but a perfect reflecting surface where compression does not occur. To express this, a mirror-image sound source $-A_0e^{-i\omega t}$ as opposed to $+A_0e^{-i\omega t}$ is assumed. The sound field at a given underwater point can be expressed as

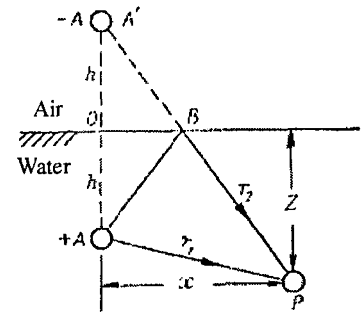

Fig. 4.3

(29) $$4\pi\phi = \frac{Ae^{+ikr_1}}{r_1} - \frac{Ae^{+ikr_2}}{r_2}$$

With respect to ϕ, the sound pressure at the interface ($z = 0$) can be expressed as

(30) $$p = p_0 + \rho\frac{\partial\phi}{\partial t} = p_0$$

so that the boundary condition $\delta p = 0$ is satisfied. If Eq. (29) is rewritten as

(31) $$4\pi\phi = Ae^{+ikr}\left\{\left(\frac{1}{r_1} - \frac{1}{r_2}\right)\cos ks - i\left(\frac{1}{r_1} + \frac{1}{r_2}\right)\sin ks\right\}$$

sound intensity is proportional to

(32) $$A_0^2\left\{\frac{1}{r_1^2} + \frac{1}{r_2^2} - \frac{1}{r_1r_2}\cos k(r_2 - r_1)\right\}$$

Let z_1 be the depth of the observation point, and x the horizontal distance from the sound source. Let us now calculate the point at which sound intensity is minimized when the depth of the sound source is large compared with the wavelength ($kh > 1$). If the sound source is distant and x is sufficiently large compared with z and h, we can assume

(33) $$r_1 = x + \frac{(z-h)^2}{2x}, \qquad r_2 = x + \frac{(z+h)^2}{2x}$$

so, we can write as

(34) $$k(r_2 - r_1) = \frac{2kh}{x}z = \frac{4\pi h}{x}\cdot\frac{z}{\lambda}$$

Hence, the point at which sound is minimized is located at the depth calculated as

(35) $$\cos k(r_2 - r_1) = +1, \qquad k(r_2 - r_1) = 0,\ 2\pi,\ 4\pi,\cdots 2n\pi,\cdots,$$

Or

(36)

$$\frac{4\pi h}{x} \cdot \frac{z}{\lambda} = 2n\pi,$$

$$z = \frac{x}{h} \cdot \frac{n\lambda}{2} \qquad (n = 0, 1, 2, 3, \cdots)$$

Sound, therefore, becomes weakest at the water surface and at depths corresponding to half wavelengths from the water surface. Needless to say, sound intensity is maximized at intermediate locations between them.

3.4.2 Distribution of sound pressure from indoor noise source

The reflection coefficient R is obtained by subtracting the absorption coefficient α from 1, that is,

$$a = 1 - R \tag{3.31}$$

In general, $S = a(1+x+x^2+\cdots) = a\sum_{n=0}^{\infty} x^n$ expresses the sum of infinite terms of a geometric series. If the ratio x is subject to the condition $0 \leq x \leq 1$, then $S = a/(1-x)$.

By using these, from Eq. (3.29), we obtain

$$I_r = cE = \frac{4P}{S}\cdot\frac{1}{\bar{\alpha}} = \frac{4P}{S}\cdot\frac{1}{1-\bar{R}} = \frac{4P}{S}\sum_{n=0}^{\infty} R^n$$
$$= \frac{4P}{S}(1+R+R^2+\cdots) \tag{3.32}$$

This equation indicates that the sound intensity (I_r) can be decomposed into the sum of infinite terms. In the equation, R^n represents the component that has been reflected n times, and 1 in the first term corresponds to the ratio of the direct sound component.

Since the intensity of direct sound from a point source is, according to Eq. (2.7), $P/4\pi r^2$, the first term ($4P/S$) of Eq. (3.32) is replaced with this. Because the second and subsequent terms of Eq. (3.32) can be written as

$$\frac{4P}{S}(R+R^2+R^3+\cdots) = \frac{4P}{S}\cdot\frac{R}{1-\bar{R}} = \frac{4P(1-\bar{\alpha})}{S\bar{\alpha}}$$

Eq. (3.32) can be rewritten as

$$I_r = \frac{P}{4\pi r^2} + \frac{4P(1-\bar{\alpha})}{\bar{\alpha}S} \tag{3.33}$$

From this, the sound pressure level can be calculated as

$$L_r = L_W + 10\log\left(\frac{Q}{4\pi r^2} + \frac{4}{R_c}\right) \tag{3.34}$$

where $R_c = \bar{\alpha}S/(1-\bar{\alpha})$ is called the "room constant," and Q is a coefficient for the direction of the sound source in relation to a wall, etc., indicating the energy concentration ratio. Examples of Q are shown in Table 3.3.

Table 3.3 Relationship between the sound source location and the direction coefficient

Sound source location relative to reflecting surface				
Direction coefficient	$Q=1$	$Q=2$	$Q=4$	$Q=8$

According to this equation, in the vicinity of a noise source, the sound pressure level decreases as the distance r from the sound source increases, but if $Q/4\pi r^2 \ll 4/R_c$ that is, $r \gg \sqrt{R_c Q/16\pi}$ then distance decay cannot be expected because of the influence of the reflected sound component [for information on Q, refer to Eq. (3.17)].

Therefore, in the range of $r \gg \sqrt{R_c Q/16\pi}$

$$\left.\begin{aligned} L_r &\fallingdotseq L_W + 10\log\frac{4}{R_c} \\ &= L_W + 6 - 10\log A - 10\log\frac{1}{1-\alpha} \end{aligned}\right\} \quad \text{(dB)} \qquad (3.35)$$

is used. Compared with Eq. (3.30), this equation gives values lower by $10\log 1/(1-\alpha)$.

The nature of Eq. (3.34) when $Q = 2$ is shown in Fig. 3.43.

Reference 1-4

Pressure Fluctuation on Self Induced Flow Oscilation Caused by Under-Expanded Super Sonic Impinging Jet

Tsuyoshi YASUNOBU, Takeshi MATSUOKA, Muneo TAGAMI and Hideo KASHIMURA,
Kitakyusyu College of Technology, Sii, Kokuraminami-ku, Kitakyusyu.

Key Words: Compressible Flow, Flow Oscillation, Super Sonic Jet, Mach Disk, Barrel Shock.

1. Introduction

Self-induced flow oscillation[1] that occurs when an underexpanded supersonic jet impinges on an object under certain conditions is an important problem from the industrial point of view, too, because such self-induced flow oscillation could cause vibration and noise[2] in, for example, high-pressure gas piping. There are many aspects, however, that require further study, such as pressure fluctuation in a flow field undergoing self-induced flow oscillation and the relationship between waves thus formed and pressure fluctuation. In this study, an experiment was conducted in which pressure fluctuation at the surface of a cylindrical body when a supersonic jet interferes with the cylindrical body was measured, and frequency analyses were conducted. This study also discusses the influence of the pressure ratio in the flow field and the position of the cylindrical body on pressure fluctuation during self-induced flow oscillation.

2. Apparatus and experiment and measurement methods

Figure 1 shows a schematic layout of the experimental apparatus used in this study. The experimental apparatus consists of a get-generating apparatus and measuring instruments. The jet-generating apparatus is composed of a compressor, a high-pressure tank, a measuring section, a vacuum tank and a vacuum pump. A jet nozzle and a cylindrical body are installed in the measuring section, and phenomena occurring during the experiment are recorded as visualized side-view image data. For the purpose of measurement, a pressure sensor (Kulite XIM-190) is installed on the cylindrical body to measure pressure fluctuation at its surface during self-induced flow oscillation. Output voltages from the pressure sensor are amplified by a direct current (DC) amplifier and recorded with a digital storage oscilloscope (Iwatsu DS-8608A), and the data are stored in a computer through a cable connected to the oscilloscope.

In the experiment, a convergent nozzle with an exit Mach number of $M_e = 1$ and an exit diameter of $D = 4$ mm and a cylindrical body having a diameter of $d_c = 12$ mm were used. The working gas used was air. In the experiment, the dimensionless distance x_c/D from the nozzle end to the cylindrical body was varied within the range of 2 to 7, and the pressure ratio ϕ in the flow field within the range of $4 \leq \phi \leq 19$.

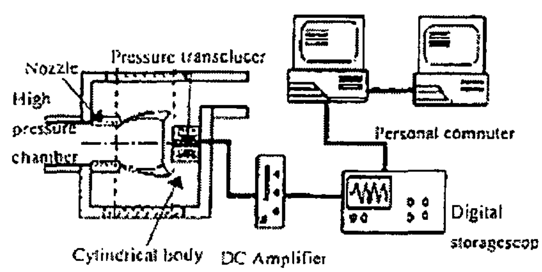

Fig. 1 Schematic layout of experimental apparatus

3. Experimental results and discussion

Figure 2 shows examples of results obtained from fast Fourier transform (FFT) analyses of the pressure waves at the surface of the cylindrical body during self-induced flow oscillation obtained from the experiment.

Figure 2 (a) shows the results obtained at $x_c/D = 5$ and $\phi = 12$. A conspicuous peak can be seen at $f =$ 9.2 kHz. For the purposes of this study, a single peak's frequency observed in a vibration frequency spectrum as in this case is defined as f_p.

Figure 2 (b) ($x_c/D = 6$, $\phi = 12$) shows a peak frequency similar to f_p shown in Fig. 2 (a), but there is also a second peak frequency (85.7 kHz). These two (lower and higher) peak frequencies are defined as f_{p1} and f_{p2}, respectively.

In Fig. 2 (c) ($x_c/D = 4$, $\phi = 4$), there is no spectrum peak as those shown in Fig. 2 (a) and (b). The spectrum shows a gradual increase at lower frequencies.

The self-induced flow oscillation observed in the experiment showed the three patterns described above. In this study, a single-peak spectrum pattern like the one shown in Fig. 2 (a) is called "pattern 1"; a two-peak pattern like the one in Fig. 2 (b), "pattern 2"; and a peakless pattern like the one in Fig. 2 (c), "pattern 3."

Figure 3 shows the relationship between the frequency peak and the pressure ratio ϕ. It shows the frequency peaks obtained from the pattern 1 and pattern 2 spectra mentioned above. According to Fig. 3, the frequency peaks f_p and f_{p1} range from 10 to 20 kHz, showing a tendency to increase slightly in proportion to the pressure ratio ϕ. Figure 3 also shows a tendency to decrease in inverse proportion to the dimensionless position x_c/D of the cylindrical body. In patterns 1 and 2, p_f and p_{f1} take similar values in all cases, while f_{p2} shows a tendency to stay nearly constant, regardless of ϕ and x_c/D. The differences between the peak frequencies f_{p1} and f_{p2} are thought to be due to differences in their generation mechanisms, but this is an area where further study is needed.

Figure 4 shows the different patterns of self-induced flow oscillation, where ①, ② and ③ represent patterns 1, 2 and 3, respectively. Under the experiment conditions, different patterns occur depending on the boundary condition of $x_c/D = 5$. When $x_c/D \leq 5$, pattern 3 occurs in the regions where the pressure ratio ϕ is low, and as the pressure ratio rises, the oscillation turns into pattern 1 oscillation. When $x_c/D > 5$, pattern 2 oscillation occurs regardless of the pressure ratio.

4. Conclusion

In this study, pressure fluctuations during self-induced oscillation of a supersonic jet impinging on a cylindrical body were measured, and frequency analysis has been discussed. The conclusions drawn from this study can be summarized as follows:

(1) The frequency of self-induced flow oscillation varied depending on the pressure ratio in the flow field and the position of the cylindrical body. This paper classified flow oscillation into three types according to the frequency spectrum distribution and showed the conditions for the occurrence of those patterns.

(2) The pattern 1 peak frequency f_p and pattern 2 peak frequency f_{p1} increased slightly in proportion to the pressure ratio ϕ and decreased in inverse proportion to the position x_c/D of the cylindrical body.

There were no significant differences between the values of f_p and f_{p1}.

(3) The pattern 2 peak frequency f_{p2} in the higher frequency range was relatively free from the influence of the pressure ratio ϕ and the position x_c/D of the cylindrical body.

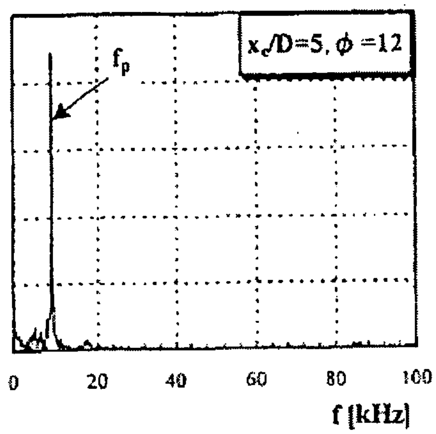

(a) x_c/D=5, ϕ=12

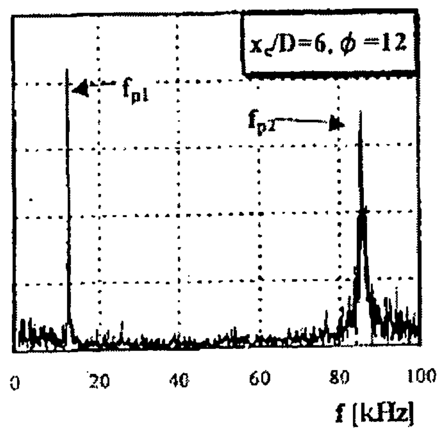

(b) x_c/D=6, ϕ=12

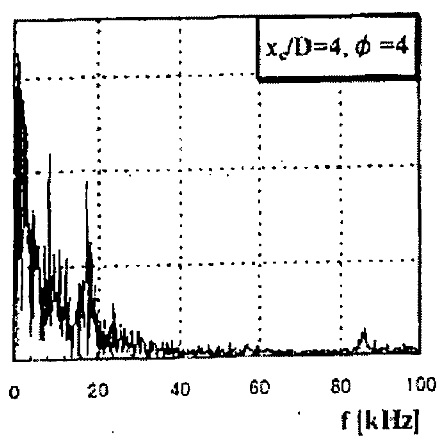

(c) x_c/D = 4, ϕ =4

Fig.2 Frequency spectrum at during flow oscillation

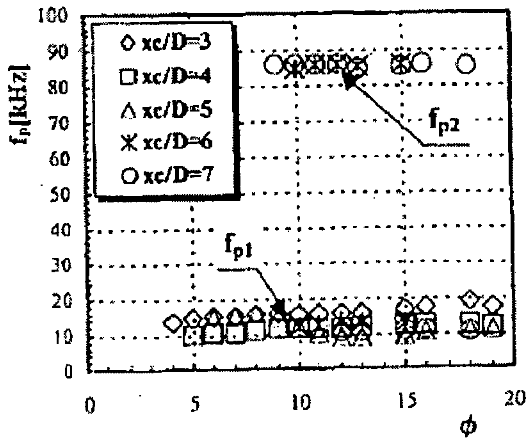

Fig.3 Relation between pressure ratio and peak frequenc

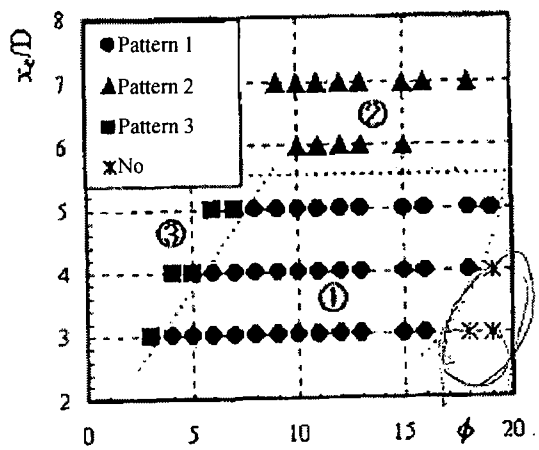

Fig.4 Relation between pressure ratio and position of cylindrical body

$\frac{D_i}{d} = 4$

References

(1) Jungowski, W. M., Some self Induced Supersonic Flow Oscillation, Prog. Aerospace Sci., Vol. 18, (1978), p. 151 - 175.

(2) Nakano, M., Outa, E. and Tajima, K., Noise and Vibration Related to the Patterns of Supersonic Annular Flow in a Pressure Reducing Gas Valvu, J. Fluids Eng., Vol. 110, (1988), p.55 - 61.

704. Steam Free Jet and Jet Impingement of High pressure Steam

By Kozo KITADE*, Tetsundo NAKATOGAWA*,
Hideo NISHIKAWA**, Kohei KAWANISHI** and Chuichi TSURUTO**

Main steam pipe break is one of the most serious accidents in PWR plant. Reaction forces, steam jet expansion and pressure on flat target on which the steam jet impinged vertically were measured. Spreading angle and area of free jet of saturated steam which was ejected from a pipe of inner diameter of 9.4 mm into atmosphere, were measured. The data are in agreement with predictions. Pressure profiles on the target on which the jet impinged vertically were measured. A distance between the nozzle exit and the target was from 5.5 to 62 mm.
Results are as follows: Reaction force is directly proportional to the ejection pressure. The pressure profile on the target varies depending on the distance between the nozzle and the target.

KEYWORDS: *main steam pipe rapture, light-water reactor, reaction forces, steam ejection, saturated steam, spreading angle, free jet of steam, impingement jet, blowdown*

I. Introduction

Safety analysis of nuclear power plants for postulated accidents is strongly required. One such accident is a break of a pressurized primary system coolant pipe or a main steam pipe, which causes a steam jet. Reactions forces from the steam jet acting on the broken pipe, a jet impinging on a structure, and the range of these forces are concerns in the strength design of structures. There are only a limited number of experiments and analyses on free and impinging jets of high-pressure steam and pressurized water, and only a few of them can be used for analysis.
We conducted an experiment on a free jet ejected and an impinging jet into air to obtain basic data on a steady-state jet of high-pressure saturated steam. This paper presents the results of the experiment. The results of the experiment on a high-pressure water jet have been reported in the previous paper (1).

II. Test apparatus and method

The test was conducted by injecting high-pressure saturated steam supplied from a factory boiler into air in the vertical direction through a test nozzle. **Fig. 1** shows the test apparatus. The nozzle for the injection of the steam was a pipe with an outer diameter of 13.8 mm and an inner diameter of 9.4 mm. An impingement plate was placed horizontally above the nozzle and subjected to an impinging jet normal to its surface. The plate was removed when a free jet was observed. The impingement plate was movable horizontally and had a 1.2 mm hole in the center for pressure measurement. A pressure transmitter was installed to the plate via a pressure pipe. The pressure profile on the impingement surface was measured by moving the plate horizontally.

* Mitsubishi At. Power Ind., Inc.
** Mitsubishi Heavy Ind., Ltd.

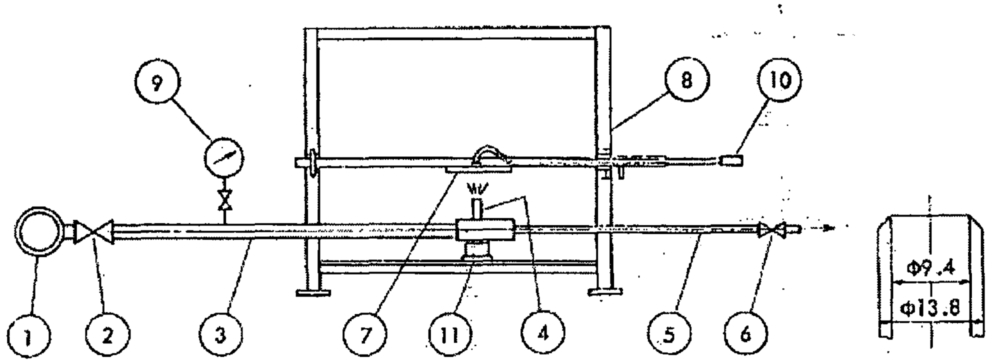

① Main steam pipe (5"), ② Valve, ③ Steam supply pipe (1"), ④ Nozzle, ⑤ Drain (1/4"), ⑥ Valve, ⑦ Target plate, ⑧ Support structure, ⑨ Pressure gauge, ⑩ Pressure transmitter, ⑪ Load cell

Fig. 1 Experimental apparatus

The distance between the nozzle and the plate was varied from 9 to 62 mm. A pressure gauge was installed on the steam supply pipe to measure the jet pressure. The jet reaction force was measured with a load cell installed at the bottom of the nozzle. The length of the steam supply pipe between the main steam pipe and the load cell was about 2 m, and the rigidity of the connection of the steam supply pipe to the main steam pipe was negligible.

III. Test results and discussion

1. Expansion of the free jet

Photo 1 shows the expansion of the free steam jet. The observation was made at a jet pressure, P_0, of 10 to 40 kg/cm^2 G.

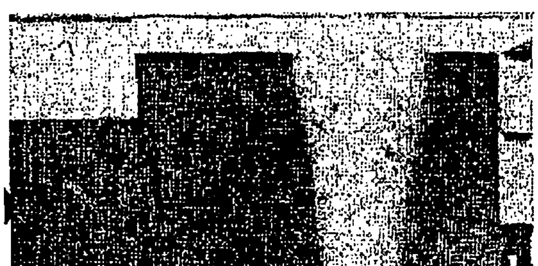

Photo. 1 Expansion of jet

When the jet of high-pressure steam is in critical state at the nozzle exit and the critical pressure is higher than atmospheric pressure, the jet is underexpanded and expands rapidly. In this case, as it is well known, the pressure profile is not uniform across the jet and has a distribution in the radial and axial directions.

Fig. 2 shows a typical internal structure of a jet. The effect of a pressure wave appears only within the jet boundary. That is, the static pressure at the jet boundary is near atmospheric pressure.

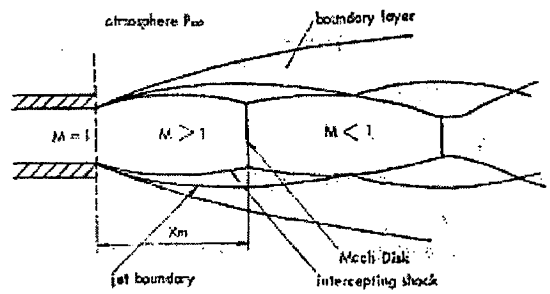

Fig. 2 Sketch of free jet structure behind highly underexpanded nozzle

A viscosity-induced boundary layer is developed outside the jet boundary, and the steam and air mix together in the boundary layer. This steam jet was photographed and its expansion was measured. **Photo 1** shows that the jet expands rapidly at the nozzle exit and then expands linearly immediately after that. The jet can be divided into two regions, Zone 1 and Zone 2. Zone 1 is where the jet expands rapidly from the nozzle exit. Zone 2 is where the jet expands linearly after the rapid expansion. As shown in **Fig. 3**, θ_1, θ_2, and A_∞ are defined as measures of this expansion.

θ_1 is the expansion angle of the jet at the nozzle exit and θ_2 is the expansion angle of the linearly expanding zone.

A_∞ is the cross-sectional area of the jet at the end of expansion to atmospheric pressure, but is difficult to define. For the sake of convenience, the expansion of the jet is divided into two modes: thermal expansion and expansion due to diffusion or viscosity. Assuming that in the second mode, the jet expands from the nozzle exit at the same rate θ_2 as in the first mode, the expansion in the first mode is obtained by subtracting the expansion in the second mode from the overall expansion. Then, the cross-sectional area A_∞ of the jet expanded to atmospheric pressure is obtained by extrapolating the expansion at θ_2 to the nozzle exit. Figs. 4 and 5 show θ_1, θ_2, and A_∞/A_E measured.

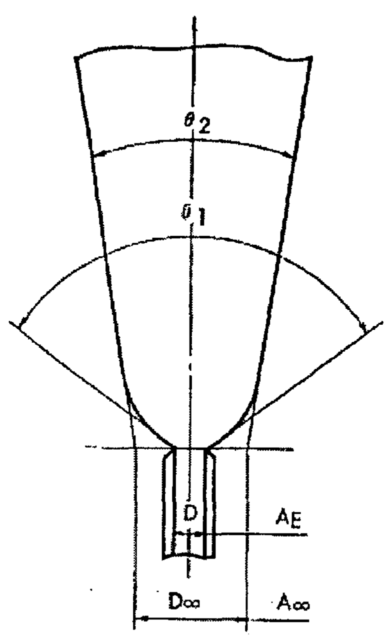

Fig. 3 Definition of θ_1, θ_2 and A_∞

(1) Expansion angle θ_1 at the nozzle exit

By approximating the underexpanded jet as a one-dimensional flow inside the nozzle and representing the jet boundary as the surface of the nozzle wall, the expansion can be considered as supersonic expansion. Assuming an ideal gas, the expansion angle θ_1 is given by the Prandtl-Meyer equation. Since the Mach number is 1 at the nozzle exit, the equation is given by equation (1). [2]

$$\frac{\theta_1}{2}=\sqrt{\frac{\kappa+1}{\kappa-1}}\tan^{-1}\sqrt{\frac{\kappa-1}{\kappa+1}(M_2^2-1)} -\tan^{-1}\sqrt{M_2^2-1} \qquad (1)$$

Where, k: adiabatic exponent (= 1.3)

M_2: Mach number

The expansion near the nozzle exit is an isentropic process and therefore meets equation (2).

$$\frac{P_0}{P_\infty}=\left(1+\frac{\kappa-1}{2}M_2^2\right)^{\kappa/(\kappa-1)} \qquad (2)$$

Where, P_0: jet pressure, P_∞: atmospheric pressure

The expansion angle calculated using equations (1) and (2) is shown in the solid line in **Fig. 4**. The measured values are slightly smaller than the calculated values, but are considered to be in general agreement with the calculation, considering the accuracy of the measurement.

(2) Expansion angle θ_2 after expansion to atmospheric pressure

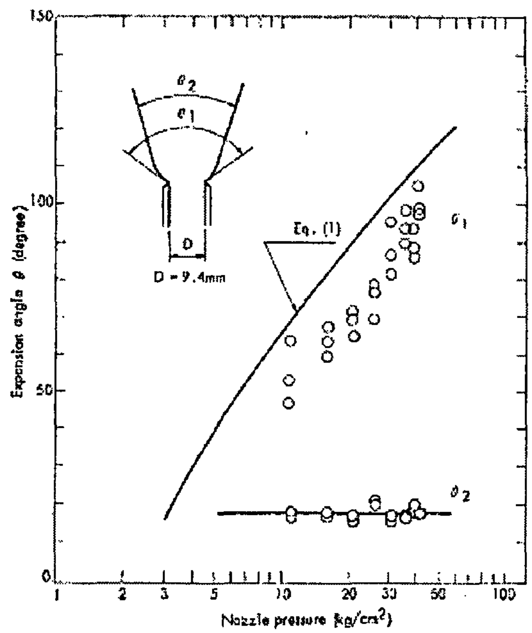

Fig. 4 Results of expansion angle

θ_2 is roughly 18 degrees and about 25 degrees smaller that the expansion angle of a general jet. The actual expansion is probably wider than this. However, the expansion area outside this angle is air and is not clearly shown in the photograph. The area shown in the photograph is probably far inside the boundary layer.

(3) Expansion area ratio

The cross-sectional area of the steam jet increases as it expands from the critical pressure at the nozzle exit to atmospheric pressure. Moody [3] proposed equation (3) to describe it.

$$\frac{A_\infty}{A_E}=\frac{v_{M\infty}}{v_{ME}}\left\{1-\frac{P_E-P_\infty}{1.26\,P_0-P_\infty}\right\} \tag{3}$$

Where, A_∞: cross-sectional area of the jet expanded to atmospheric pressure

A_E: cross-sectional area of the nozzle

v_{ME}: specific volume in the nozzle

$v_{M\infty}$: specific volume after expansion

P_0: nozzle jet pressure

P_∞: atmospheric pressure

$v_{M\infty}$ is calculated using equation (4).

$$v_{M\infty}=x_\infty v_{g\infty}+(1-x_\infty)v_{l\infty} \tag{4}$$

Where, x_∞: quality of the jet expanded to atmospheric pressure

$v_{g\infty}$: specific volume of saturated steam at atmospheric pressure

$v_{l\infty}$: specific volume of saturated water at atmospheric pressure

Assuming an isentropic change, x_∞ is given by equation (5).

$$x_\infty=\frac{s_0-s_l}{s_g-s_l} \tag{5}$$

Where, s_0: entropy of saturated steam at the jet pressure

s_l: entropy of saturated water at atmospheric pressure

s_g: entropy of saturated steam at atmospheric pressure

v_{ME} is calculated using equation (6) of critical state of ideal gas.

$$\frac{v_{ME}}{v_0}=\left(1+\frac{\kappa-1}{2}\right)^{1/(\kappa-1)} \tag{6}$$

Where, v_0: specific volume of saturated steam at the jet pressure

Fig. 5 shows jet expansion calculated for an isenthalpic change and an isentropic change using equation (3).

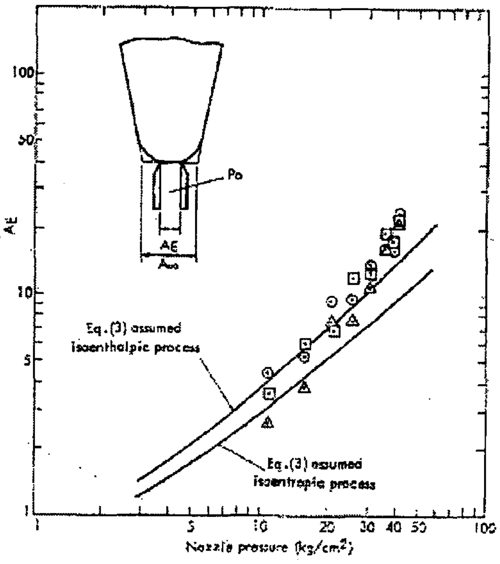

Fig. 5 Results of jet expansion

The measured values are close to the calculated values. This is probably due to the presence of a shock wave in the jet and increased entropy from friction with the air.

2. Impinging jet

(1) Pressure profile on the impingement plate

The pressure profile on the plate subjected to an impinging jet normal to its surface was measured in the following conditions.

Nozzle diameter D = 9.4 mm

Nozzle-impingement plate distance H = 5.5 to 62 mm

Jet pressure P_0 = 11 to 41 kg/cm^2

The pressure profile on the impingement plate depends on the distance and can be largely divided into three patterns as shown in **Fig. 6**. **Fig. 7** shows the results of the measurement of the pressure profile. When the plate is close to the nozzle, or when *H/D* is small, the pressure profile on the plate is shaped like Type 1. As the distance from the nozzle increases, the pressure at the center of the plate decreases, and the pressure profile changes from Type 1 to Type 2 to a trapezoidal shape and eventually to Type 3, which is concave in the center. This is agreement with the experiment results of Kuboki et al. [4] using air.

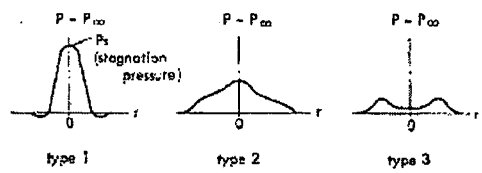

Fig. 6 Sketch of pressure distribution on target plate

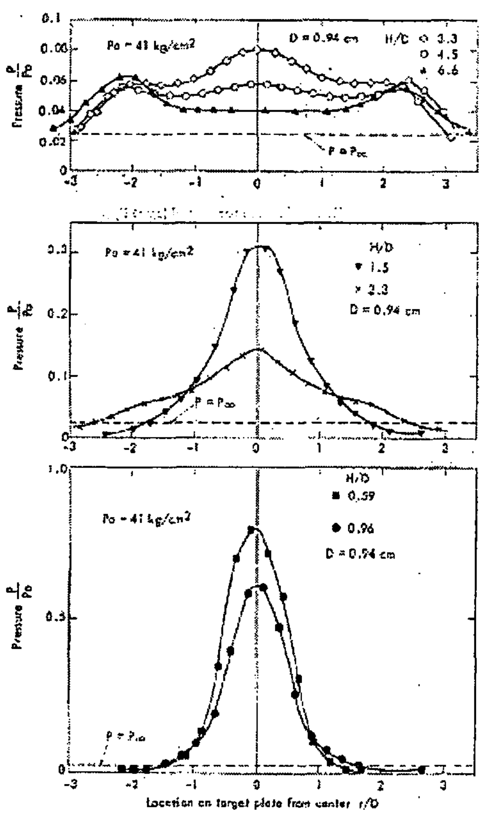

Fig. 7 Pressure distribution on target plate

The center of the impingement plate is a stagnation point and the point of the highest pressure, except Type 3. **Fig. 8** shows the relationship between the pressure at the stagnation point P_s and the dimensionless distance *H/D*, which is given by equation (7) for *H/D* more than 1, regardless of the jet pressure. It is in general agreement with experimental results of Stitt [5] using air.

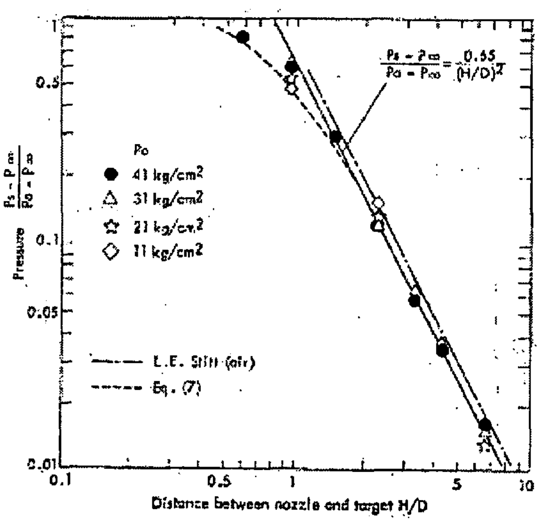

Fig. 8 Pressure at center of target plate

$$\frac{P_s - P_\infty}{P_0 - P_\infty} = 0.65\left(\frac{H}{D}\right)^{-2.0}, \quad (H/D > 1) \tag{7}$$

Owen et al. [6] calculated the axial variation in the Mach number of a free jet underexpanded into vacuum for an exit Mach number of 1.008, using the characteristic curve method. The calculation results are shown in **Fig. 9**.

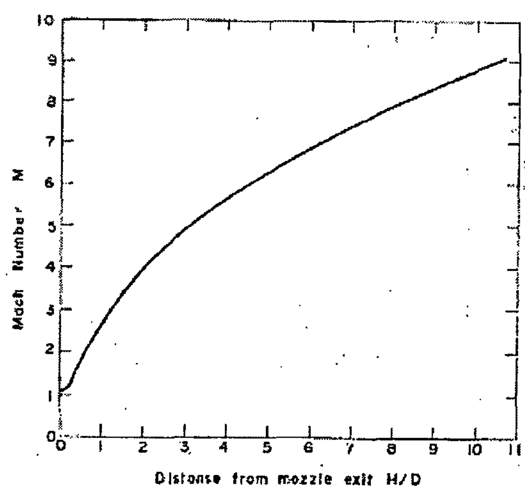

Fig. 9 Axial variation of Mach number along centerline of flow from sonic orifice into vacuum (Owen & Thornhill[6])

For smaller H/D, a vertical shock wave is generated in front of the impingement plate [4], suggesting that the pressure at the center of the plate is equal to the total pressure downstream of the shock wave. Assuming an isentropic flow upstream of the shock wave, the ratio of the pressure at the center of the plate and the jet pressure is given by equation (8) for the relationship of the total pressures behind and in front of the vertical shock wave. [2]

$$\frac{P_s}{P_0}=\left[1+\frac{2\kappa}{\kappa+1}(M_1^2-1)\right]^{-1/(\kappa-1)} \cdot\left[\frac{(\kappa+1)M_1^2}{(\kappa-1)M_1^2+2}\right]^{\kappa/(\kappa-1)} \tag{8}$$

Where, M_1: Mach number immediately upstream of the impingement plate

The axial variation in P_s/P_0 can be calculated from the axial variation in Mach number in Fig. 9 and equation (8). The calculated variation is shown in the dashed line in Fig. 8. The calculation results are in good agreement with the experimental results.

The pressure profile on the impingement plate changes to Type 3 for larger *H/D*. In Type 3, the point of the highest pressure is located not in the center but on the circle along the periphery of the plate. The pressure at the center of the plate decreases with increasing *H/D* while the highest pressure on the circle remains nearly constant for *H/D* of 3.3 to 6.6.

Fig. 10 shows the dimensionless distance $(H/D)_{C2}$ between the nozzle and the impingement plate at which the pressure profile changes from Type 2 and Type 3. $(H/D)_{C2}$ is given by equation (9).

$$(H/D)_{c2}=0.72\sqrt{P_0-P_\infty} \tag{9}$$

The pressure profile at this point is intermediate between Type 2 and Type 3 and nearly trapezoidal shaped.

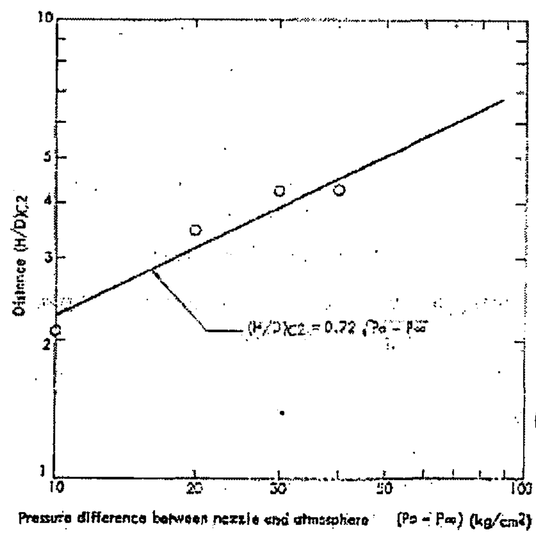

Fig. 10 Distance at which pressure profile on target varies from Type 2 to Type 3

(2) Expansion of the pressure profile

Fig. 11 shows the pressure profile represented by half-value radius $\tau_{1/2}$. The half-value radius is defined as the distance from the center of the point where the pressure is a half of the highest pressure. The dependence of the half-radius on *H/D* is divided into three regions as shown in Fig. 11. The pressure profile in each region corresponds to Type 1, Type 2 and Type 3 in Fig. 6.

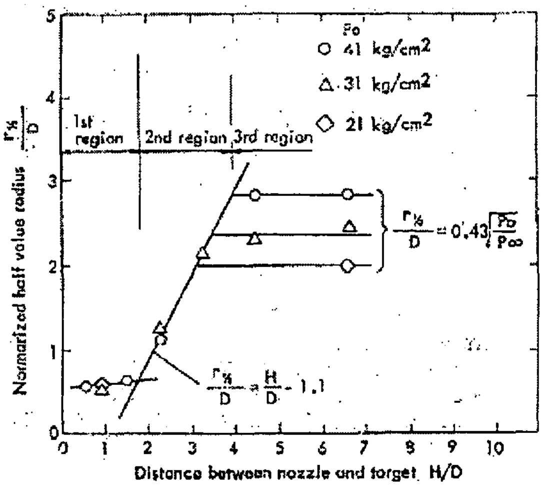

Fig. 11 Half value radius of pressure profile on target plate

Region 1: Fig. 12 shows the pressure profile near the center. The pressure profile is similarly shaped, independent of *H/D*, and is given by equation (10). [7]

$$\frac{P-P_\infty}{P_s-P_\infty}=\mathrm{sech}^2\left(0.88\frac{r}{r_{1/2}}\right) \tag{10}$$

The pressure at the stagnation point P_s in the region close to the nozzle is given by

$$P_s \doteq P_0, \quad H/D<0.8 \tag{11}$$

Equation (8) is applied to the region up to the boundary $(H/D)_{C1}$ between Region 1 and Region 2. The threshold value $(H/D)_{C1}$ is given by equation (12).

$$(H/D)_{C1} \doteq 1.8 \tag{12}$$

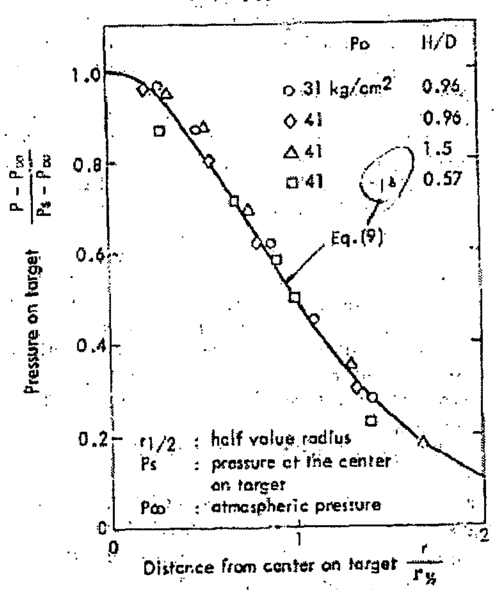

Fig. 12 Pressure profile on target plate (Type 1)

Region 2: The pressure profile is not similarly shaped and changes from a flat shape to a trapezoidal shape as *H/D* increases. The pressure at the center is given by equation (7). The half-value radius is proportional to *H/D* and given by equation (13).

$$\frac{r_{1/2}}{D}=\frac{H}{D}-1.1 \tag{13}$$

Region 3: The pressure profile has two peaks. The half-value radius is nearly constant independent of *H/D*, but is a function of the jet pressure and given by equation (14).

$$\frac{r_{1/2}}{D}=0.43\left(\frac{P_0}{P_\infty}\right)^{1/2} \tag{14}$$

The highest pressure is nearly constant at 2.5 kg/cm^2 independent of the jet pressure.

(3) Pipe reaction forces

The pipe reaction forces from a free jet and an impinging jet are nearly the same for *H/D*>1. **Fig. 13** shows the relationship between the jet pressure and the pipe reaction force, which is give by equation (15).

$$\frac{T}{(P_0-P_\infty)A_E}=1.12 \tag{15}$$

Where, T: pipe reaction force (kg)

A_E: nozzle area (cm^2)

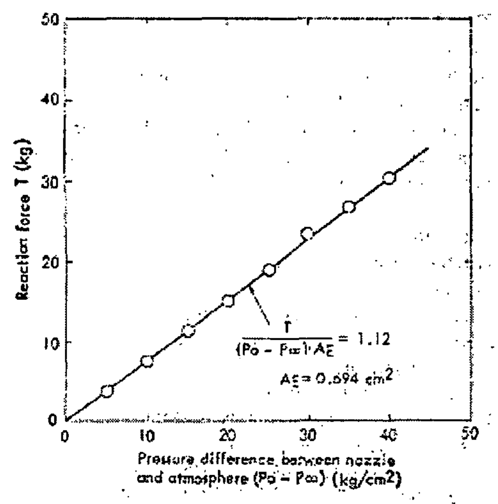

Fig. 13 Results of reaction force

The right term in equation (15) is called thrust coefficient. In Moody's analysis, the thrust coefficient is 1.26 for a frictionless flow. A possible reason for this difference is the use of a pipe (110 mm long, 9.4 mm in inner diameter) for the nozzle exit and, as a result, the influence of pressure loss and the contraction flow at the pipe inlet. Further study is required to identify the reason.

IV. Conclusions

We conducted an experiment on a free jet and an impinging jet and obtained the following conclusions.

(1) A free jet was observed and data on its expansion angle and area were obtained.

(2) The pressure profile significantly varies with the distance *H* when a jet impinging on the plate vertically. A test was conducted for the ratio *H/D* of the distance *H* to the diameter *D* of the nozzle exit smaller than 6.6. Data on the expansion of the pressure profile and the point and value of the highest pressure were obtained. The dependence of the pressure profile on *H/D* can be divided into three regions. At the moment, the test apparatus is being modified to obtain data for *H/D* larger than 6.6. The results of a test using the modified apparatus will be presented in the next report.

(3) For smaller *H/D*, the measured pressure at the center of the impingement plate is in agreement with the calculation using the equation for the relationship with a vertical shock wave based on the calculation results of Owen et al.

(4) The thrust coefficient for the reaction force was 1.12 in the test apparatus used. This is in disagreement with the analysis results of Moody. This disagreement is probably due to the influence of the contraction flow at the nozzle inlet. Further study is required.

References

(1) Kitade, K., et al.: Journal of Nuclear Energy, 22 (5), 343, (1980).

(2) Liepmann, H.W., Roshko, A.: "Elements of Gas-dynamics", 61 (1960), John Wiley & Sons.

(3) Moody, F.J.: ASME 69-HT-31, (1969).

(4) Kuboki, Y, et al.: Proceedings of the 9th Japan Heat Transfer Symposium, 249 (1972)

(5) Stitt, L.E.: NASA TN-D-1095, (1961)

(6) Owen, P.l., Thronhill, C.K.: Brit. ARC Tech. Rep., R & M 2616, (1952)

(7) Nakatogawa, T.: Proceedings of the 7th Japan Heat Transfer Symposium, 53 (1970)

Reference 2-9

Pressure Fluctuation on Self Induced Flow Oscilation Caused by Under-Expanded Super Sonic Impinging Jet

Tsuyoshi YASUNOBU, Takeshi MATSUOKA, Muneo TAGAMI and Hideo KASHIMURA,
Kitakyusyu College of Technology, Sii, Kokuraminami-ku, Kitakyusyu.

Key Words: Compressible Flow, Flow Oscillation, Super Sonic Jet, Mach Disk, Barrel Shock.

1. Introduction

Self-induced flow oscillation[1] that occurs when an underexpanded supersonic jet impinges on an object under certain conditions is an important problem from the industrial point of view, too, because such self-induced flow oscillation could cause vibration and noise[2] in, for example, high-pressure gas piping. There are many aspects, however, that require further study, such as pressure fluctuation in a flow field undergoing self-induced flow oscillation and the relationship between waves thus formed and pressure fluctuation. In this study, an experiment was conducted in which pressure fluctuation at the surface of a cylindrical body when a supersonic jet interferes with the cylindrical body was measured, and frequency analyses were conducted. This study also discusses the influence of the pressure ratio in the flow field and the position of the cylindrical body on pressure fluctuation during self-induced flow oscillation.

2. Apparatus and experiment and measurement methods

Figure 1 shows a schematic layout of the experimental apparatus used in this study. The experimental apparatus consists of a get-generating apparatus and measuring instruments. The jet-generating apparatus is composed of a compressor, a high-pressure tank, a measuring section, a vacuum tank and a vacuum pump. A jet nozzle and a cylindrical body are installed in the measuring section, and phenomena occurring during the experiment are recorded as visualized side-view image data. For the purpose of measurement, a pressure sensor (Kulite XIM-190) is installed on the cylindrical body to measure pressure fluctuation at its surface during self-induced flow oscillation. Output voltages from the pressure sensor are amplified by a direct current (DC) amplifier and recorded with a digital storage oscilloscope (Iwatsu DS-8608A), and the data are stored in a computer through a cable connected to the oscilloscope.
In the experiment, a convergent nozzle with an exit Mach number of $M_c = 1$ and an exit diameter of $D = 4$ mm and a cylindrical body having a diameter of $d_c = 12$ mm were used. The working gas used was air. In the experiment, the dimensionless distance x_c/D from the nozzle end to the cylindrical body was varied within the range of 2 to 7, and the pressure ratio ϕ in the flow field within the range of $4 \leq \phi \leq 19$.

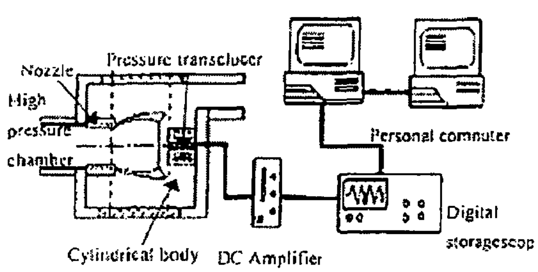

Fig.1 Schematic layout of experimental apparatus

3. Experimental results and discussion

Figure 2 shows examples of results obtained from fast Fourier transform (FFT) analyses of the pressure waves at the surface of the cylindrical body during self-induced flow oscillation obtained from the experiment.

Figure 2 (a) shows the results obtained at x_c/D = 5 and ϕ = 12. A conspicuous peak can be seen at f = 9.2 kHz. For the purposes of this study, a single peak's frequency observed in a vibration frequency spectrum as in this case is defined as f_p.

Figure 2 (b) (x_c/D = 6, ϕ = 12) shows a peak frequency similar to f_p shown in Fig. 2 (a), but there is also a second peak frequency (85.7 kHz). These two (lower and higher) peak frequencies are defined as f_{p1} and f_{p2}, respectively.

In Fig. 2 (c) (x_c/D = 4, ϕ = 4), there is no spectrum peak as those shown in Fig. 2 (a) and (b). The spectrum shows a gradual increase at lower frequencies.

The self-induced flow oscillation observed in the experiment showed the three patterns described above. In this study, a single-peak spectrum pattern like the one shown in Fig. 2 (a) is called "pattern 1"; a two-peak pattern like the one in Fig. 2 (b), "pattern 2"; and a peakless pattern like the one in Fig. 2 (c), "pattern 3."

Figure 3 shows the relationship between the frequency peak and the pressure ratio ϕ. It shows the frequency peaks obtained from the pattern 1 and pattern 2 spectra mentioned above. According to Fig. 3, the frequency peaks f_p and f_{p1} range from 10 to 20 kHz, showing a tendency to increase slightly in proportion to the pressure ratio ϕ. Figure 3 also shows a tendency to decrease in inverse proportion to the dimensionless position x_c/D of the cylindrical body. In patterns 1 and 2, p_f and p_{f1} take similar values in all cases, while f_{p2} shows a tendency to stay nearly constant, regardless of ϕ and x_c/D. The differences between the peak frequencies f_{p1} and f_{p2} are thought to be due to differences in their generation mechanisms, but this is an area where further study is needed.

Figure 4 shows the different patterns of self-induced flow oscillation, where ①, ② and ③ represent patterns 1, 2 and 3, respectively. Under the experiment conditions, different patterns occur depending on the boundary condition of x_c/D = 5. When $x_c/D \leq 5$, pattern 3 occurs in the regions where the pressure ratio ϕ is low, and as the pressure ratio rises, the oscillation turns into pattern 1 oscillation. When $x_c/D > 5$, pattern 2 oscillation occurs regardless of the pressure ratio.

4. Conclusion

In this study, pressure fluctuations during self-induced oscillation of a supersonic jet impinging on a cylindrical body were measured, and frequency analysis has been discussed. The conclusions drawn from this study can be summarized as follows:

(1) The frequency of self-induced flow oscillation varied depending on the pressure ratio in the flow field and the position of the cylindrical body. This paper classified flow oscillation into three types according to the frequency spectrum distribution and showed the conditions for the occurrence of those patterns.

(2) The pattern 1 peak frequency f_p and pattern 2 peak frequency f_{p1} increased slightly in proportion to the pressure ratio ϕ and decreased in inverse proportion to the position x_c/D of the cylindrical body.

There were no significant differences between the values of f_p and f_{p1}.

(3) The pattern 2 peak frequency f_{p2} in the higher frequency range was relatively free from the influence of the pressure ratio ϕ and the position x_c/D of the cylindrical body.

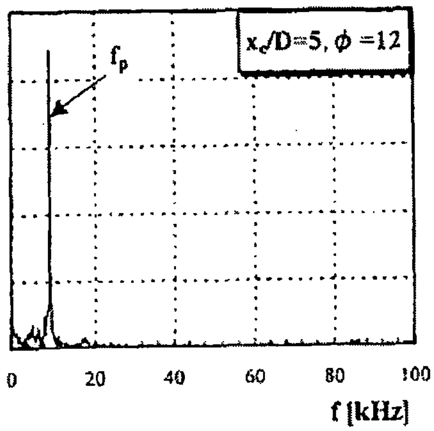

(a) x_c/D=5, ϕ=12

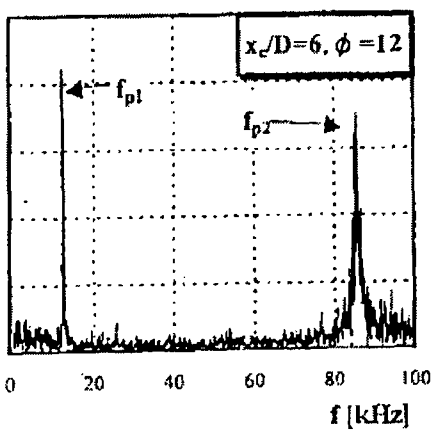

(b) x_c/D=6, ϕ=12

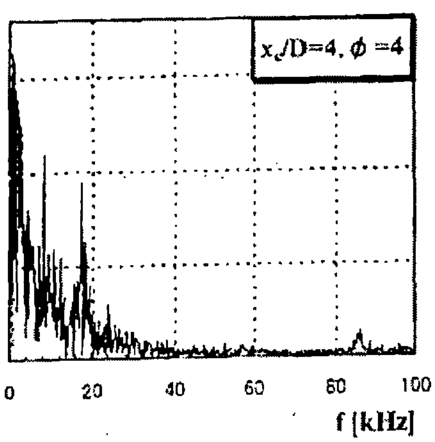

(c) x_c/D = 4, ϕ=4

Fig.2 Frequency spectrum at during flow oscillation

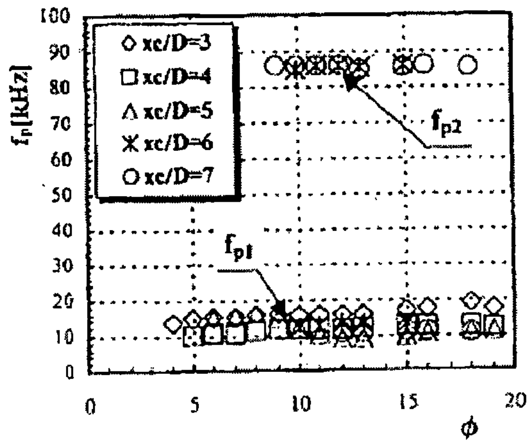

Fig.3 Relation between pressure ratio and peak frequenc

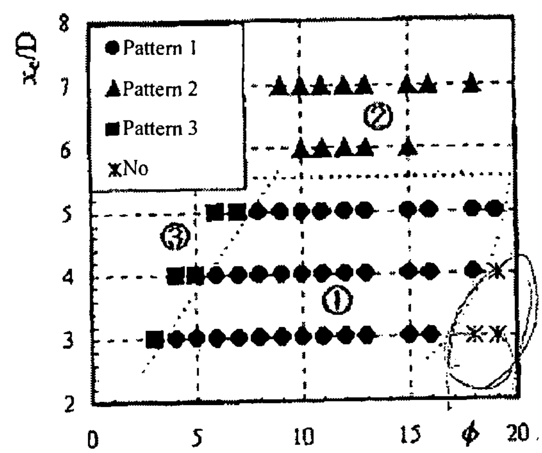

Fig.4 Relation between pressure ratio and position of cylindrical body

$\frac{D_i}{d} = 4$

References

(1) Jungowski, W. M., Some self Induced Supersonic Flow Oscillation, Prog. Aerospace Sci., Vol. 18, (1978), p. 151 - 175.

(2) Nakano, M., Outa, E. and Tajima, K., Noise and Vibration Related to the Patterns of Supersonic Annular Flow in a Pressure Reducing Gas Valvu, J. Fluids Eng., Vol. 110, (1988), p.55 - 61.

11.5 Radial wall jets produced by impinging jets (1)

Suppose a cylindrical nozzle of diameter d (= 2_{b0}) is placed at a normal distance of H from a smooth-surfaced circular plate with a large diameter as shown in Fig. 11.6. The jet from the nozzle normally on the circular plate and spreads radially outward as a radial wall jet. Experiments on this type of radial wall jet have been conducted by Poreh and Cermak (1959), Bradshow and Love (1961), Tani and Komatsu (1964), Poreh et al. (1967) and Beltaos and Rajaratnam (1974).

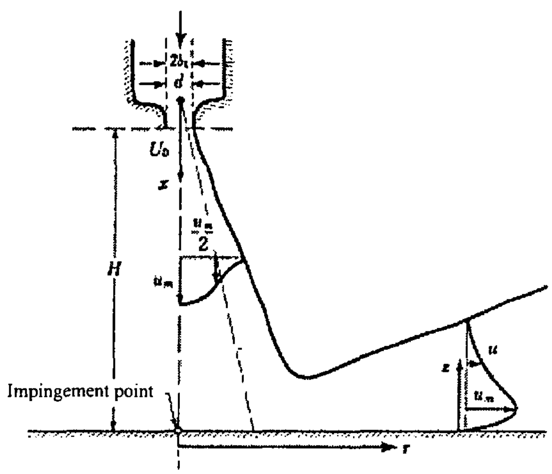

Fig. 11.6 Radial wall jet produced by axisymmetric impinging jets

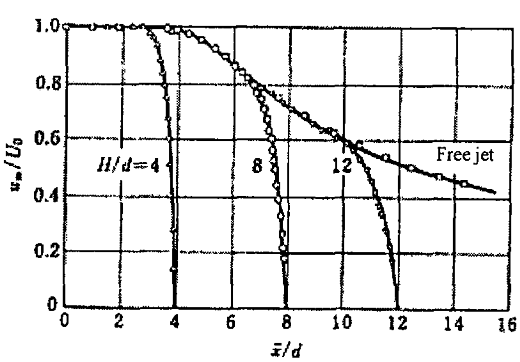

Fig. 11.7 Changes in center-line velocity of axisymmetric impinging jets (Tani and Komatsu, 1964)

Figure 11.6 suggests that the presence of the wall should slow down the impinging jets near the wall. Figure 11.7, reproduced from Tani and Komatsu, illustrates this point vividly. The experimental results of Beltaos and Rajaratnam (1974) indicate that the jet is affected by the wall when, $\bar{x}/H > 0.86$

where $\bar{x}$ is the axial distance measured from the nozzle. Let p_s be the difference between the stagnation pressure at the point of impingement on the wall and the atmospheric pressure, the following equation holds true:

$$p_s = \frac{50}{\left(\frac{H}{d}\right)^2}\frac{\rho U_0^2}{2} \tag{11.22}$$

Typical pressure distributions near the impingement point, reproduced from Tani and Komatsu (1964), are shown in Fig. 11.8. The pressure distributions near the impingement point are very closely approximated by stagnation flow solutions. Beltaos and Rajaratnam (1974) showed that the pressure distribution on the wall could be expressed as

$$\frac{p_w}{p_s} = \exp\left\{-114\left(\frac{r}{H}\right)^2\right\} \tag{11.23}$$

where p_w is the excess wall pressure above the atmospheric pressure.

Figure 11.9 shows changes in wall frictional stress τ_0 dependent on the diameter r. As shown, the wall frictional stress increases in proportion to r and reaches a maximum value at $r/H \approx 0.14$ and then decreases as r increases. Beltaos and Rajaratnam (1974) found that changes in wall frictional stress can be expressed as

$$\frac{\tau_0}{\tau_{0m}} = 0.18\left[\frac{1-\exp\left\{-114\left(\frac{r}{H}\right)^2\right\}}{\frac{r}{H}}\right] - 9.43\left(\frac{r}{H}\right)\exp\left\{-114\left(\frac{r}{H}\right)^2\right\} \tag{11.24}$$

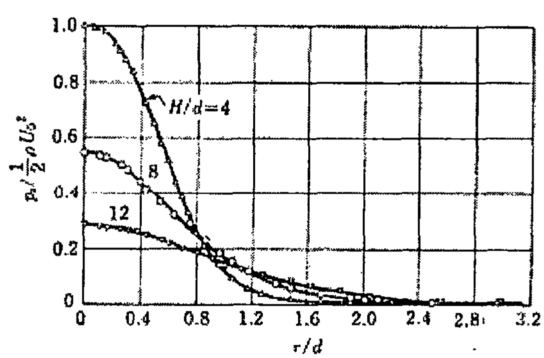

Fig. 11.8 Static pressure distribution on the wall (Tani and Komatsu, 1964)

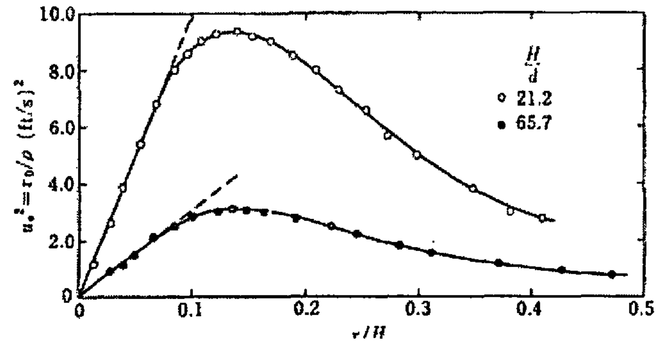

Fig. 11.9 Wall frictional stress distribution curves (Beltaos and Rajaratnam, 1974)

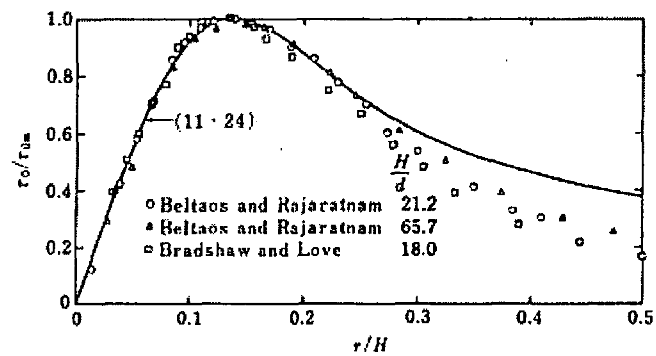

Fig. 11.10 Dimensionless wall frictional stress distribution curve (Beltaos and Rajaratnam, 1974)

where the maximum frictional stress τ0m can be expressed as

$$\tau_{0m} = 0.16\frac{\rho U_n^2}{\left(\frac{H}{d}\right)^2} \tag{11.25}$$

The relations for impinging jets derived in this section are thought to be valid only when the impingement height is large, that is, when $H/d > 8$.

11.6 Radial wall jets produced by impinging jets (2)

Flow occurring at distances greater than a certain limit from the wall is thought to be in the state of a single wall jet as shown in Fig. 11.11. It has been found that when plotted in the form of the u/u_m–z/b relationship, these curves are similar (see Figs. 11.12). The experimental results of Poreh at al. (1967) and Bradshow and Love (1961) are shown in Fig. 11.13 in the form of the $1/u_m$–r relationship. It has been found that $u_m \propto 1/r$ if the virtual origin is located at a distance of 2.5 inches from the center. The experimental points obtained by Poreh et al. (1967) are plotted in Fig. 11.14 as U_0/u_m against r/d. It can be seen that these points can be described by a single straight line. In this case, the amount of correction for the virtual origin is negligibly small. The straight-line equation, therefore, can be reduce to the form

$$\frac{u_m}{U_0} = \frac{1.03}{\frac{r}{d}} \tag{11.26}$$

It is interesting to note that the height of the impingement jet does not appear in Eq. (11.26). Examination of the data reveals that H/d varies from 8 to 24. This result shows very close agreement with the early research results of Poreh and Cermak (1959), which showed an average value of H/d of 16.2 (while H varied from 1.39 ft to 2.0 ft). This can be explained as follows.

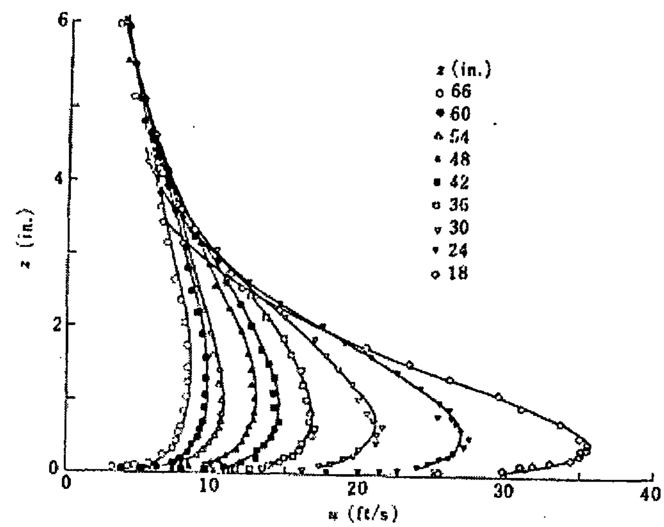

Fig. 11.11 Velocity distribution of radial wall jets produced by axisymmetric impinging jets (Tsuei, 1962)

First of all, we have the following relation:

$$u_m = f_1(M_0, \rho, H, r) \tag{11.27}$$

By using π-theorem, we have

$$\frac{u_m}{\sqrt{\frac{M_0}{\rho H^2}}} = f_1\left(\frac{r}{H}\right) \tag{11.28}$$

Because early theoretical discussions as well as the experimental results indicated $u_m \propto 1/r$, the above equation can be further rewritten as

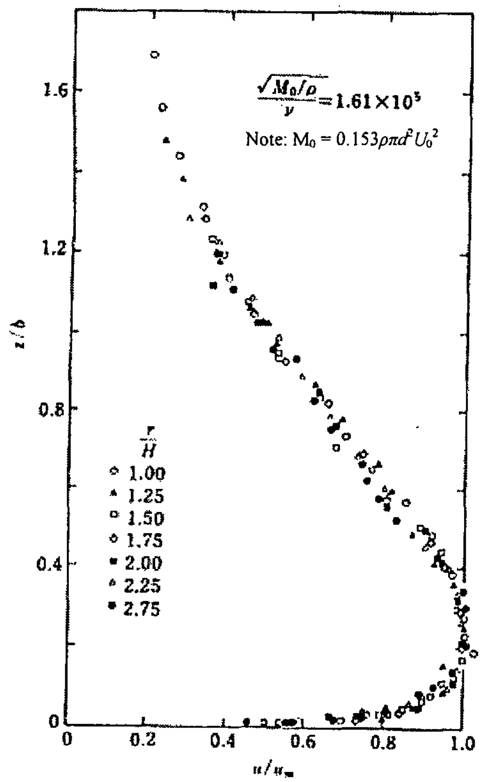

Fig. 11.12 Dimensionless velocity distribution of radial wall jets produced by axisymmetric impinging jets (Poreh et al., 1967)

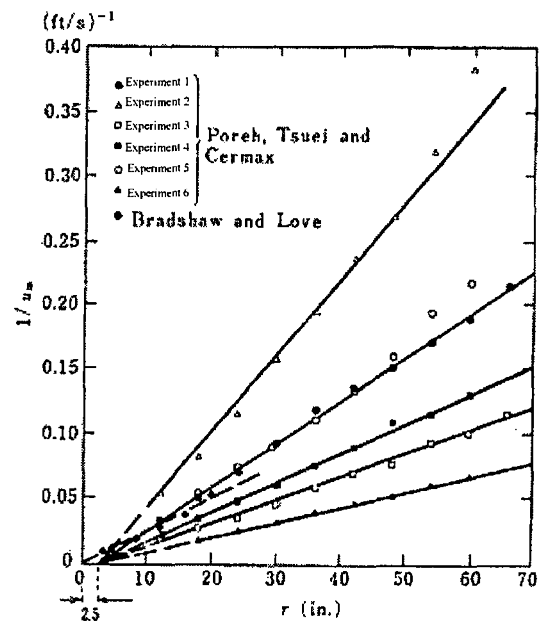

		d(in)	H(ft)	U_0(ft/s)
Poreh et al.	Experiment 1	1	2	370
	Experiment 2	1	2	223
	Experiment 3	2	2	340
	Experiment 4	2	2	279
	Experiment 5	2	2	174
	Experiment 6	3	2	333
Bradshow and Love		1	1.5	350

Fig. 11.13 Velocity scale for radial wall jets produced by axisymmetric impinging jets

$$\frac{u_m}{\sqrt{\frac{M_0}{\rho H^3}}} \propto \frac{1}{\frac{r}{H}} \tag{11.29}$$

This explains the disappearance of H.

Changes in the length scale b are shown in Fig. 11.15 in the form of the b–r relationship by using the data of Poreh et al. As expected, the changes are fairly linear, and the virtual origin is, on average, located on the center line. The length scale can be expressed as

$$b = 0.087\, r \tag{11.30}$$

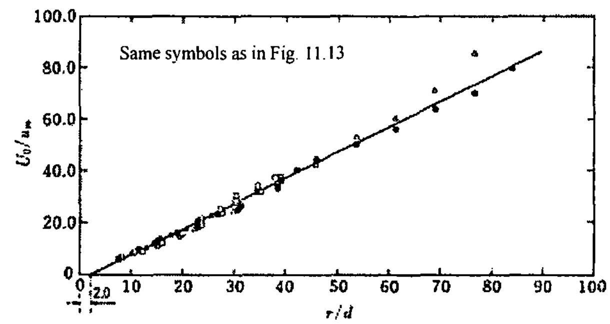

Fig. 11.14 Correlations of length scales for radial wall jets produced by axisymmetric impinging jets

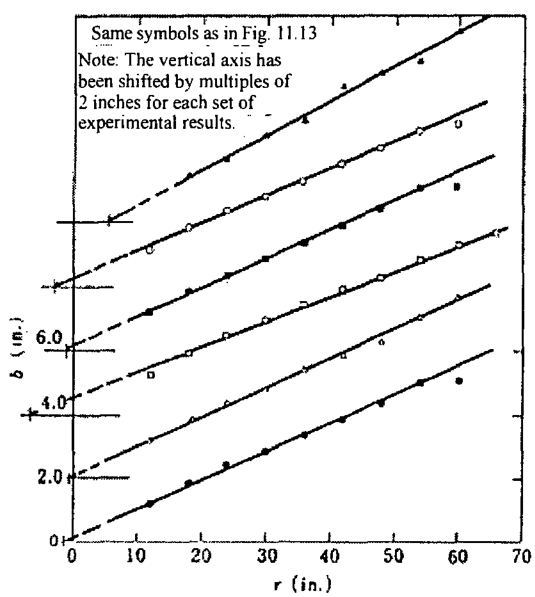

Fig. 11.15 Length scale for radial wall jets produced by axisymmetric impinging jets

As we have discussed earlier concerning the wall frictional stress τ_0, for radial wall jets, $\tau_x \propto 1/r^2$, that is, $u_* \propto 1/r$ holds true, where u_* is the frictional velocity. The experimental results of Poreh, Tsuei and Cermak (1967) are shown in Fig. 11.16 in the form of the relationship between $1/u_*$ and r. The changes are indeed linear with the virtual origin located very close to the center. Now, we can write

$$\tau_0 = f_1(M_0, \rho, H, r) \tag{11.31}$$

Neglecting the effects of viscosity. The above equation can also be written as

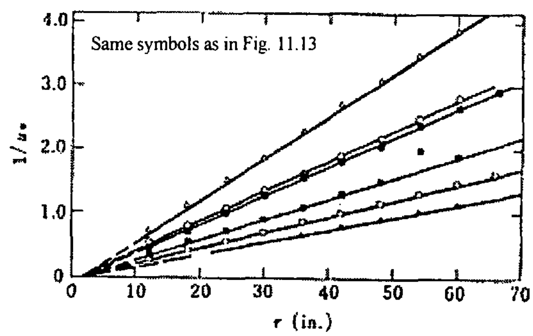

Fig. 11.16 Wall frictional stress in radial wall jets produced by axisymmetric impinging jets

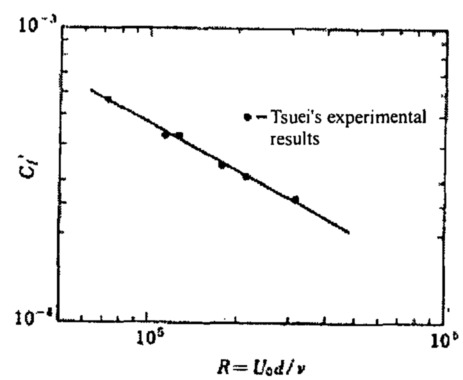

Fig. 11.17 Changes in c'_f with Reynolds number for radial wall jets produced by axisymmetric impinging jets

$$\frac{\tau_0}{\frac{M_0}{H^2}} = f_2\left(\frac{r}{H}\right) \tag{11.32}$$

Because $\tau_0 \propto 1/r^2$, Eq. (11.32) can be rewritten as

$$\frac{\tau_0}{\frac{M_0}{H^2}} \propto \frac{1}{\left(\frac{r}{H}\right)^2} \tag{11.33}$$

or

$$\frac{\tau_0}{M_0} \propto \frac{1}{r^2} \tag{11.34}$$

By using Eq. (11.16), the above can be rewritten as

$$c_f = \frac{\tau_0}{\frac{\rho U_0^2}{2}} = \frac{c'_f}{\left(\frac{r}{d}\right)^2} \tag{11.35}$$

where c'_f is a coefficient equal to $\tau_0 \Big/ \left(\frac{1}{2}\rho u_m^2\right)$ which has been found to be a function of the Reynolds number $R = U_0 d/\nu$. Changes in c'_f are shown in Fig. 11.17 and can be expressed as

$$c'_f = \frac{0.238}{R^{0.34}} \tag{11.36}$$

Docket No. 52-021
MHI Ref: UAP-HF-11028

ATTACHMENT 1

FILES CONTAINED IN CDs

CD 1: Technical Report, MUAP-10022-P (R1) "Evaluation on Jet Impingement Issues Associated with Postulated Pipe Rupture (Proprietary)"

Contents of CD

File Name	Size	Sensitivity Level
MUAP-10022-P_R0_JET.pdf	20.2MB	Proprietary

CD 2: Technical Report, MUAP-10017-NP (R1) "Evaluation on Jet Impingement Issues Associated with Postulated Pipe Rupture (Non-Proprietary)"

Contents of CD

File Name	Size	Sensitivity Level
MUAP-10022-NP_R0_JET.pdf	0.2MB	Non-Proprietary